



1

2

## 3 Top of the Atmosphere Reflected Shortwave Radiative Fluxes from GOES-R

4

5 Rachel T. Pinker<sup>1</sup>, Yingtao Ma<sup>1</sup>, Wen. Chen<sup>1</sup>, Istvan Laszlo<sup>2</sup>, Hongqing Liu<sup>3</sup>,

6 Hye-Yun Kim<sup>3</sup> and Jamie Daniels<sup>2</sup>

7 <sup>1</sup>Department of Atmospheric and Oceanic Science, University of Maryland, College Park, MD

8 <sup>2</sup>NOAA NESDIS Center for Satellite Applications and Research, College Park, MD

9 <sup>3</sup>I.M. Systems Group, Inc., Rockville, MD

10 Correspondence to: Rachel T. Pinker ([pinker@atmos.umd.edu](mailto:pinker@atmos.umd.edu))

11

12 **Abstract.** Under the GOES-R activity, new algorithms are being developed at the National Oceanic and  
13 Atmospheric Administration (NOAA)/Center for Satellite Applications and Research (STAR) to derive  
14 surface and Top of the Atmosphere (TOA) shortwave (SW) radiative fluxes from the Advanced Baseline  
15 Imager (ABI), the primary instrument on GOES-R. This paper describes a support effort in the  
16 development and evaluation of the ABI instrument capabilities to derive such fluxes. Specifically, scene  
17 dependent narrow-to-broadband (NTB) transformations are developed to facilitate the use of observations  
18 from ABI at the TOA. Simulations of NTB transformations have been performed with MODTRAN4.3  
19 using an updated selection of atmospheric profiles as implemented with the final ABI specifications.  
20 These are combined with Angular Distribution Models (ADMs), which are a synergy of ADMs from the  
21 Clouds and the Earth's Radiant Energy System (CERES) and from simulations. Surface condition at the  
22 scale of the ABI products as needed to compute the TOA radiative fluxes come from the International  
23 Geosphere-Biosphere Programme (IGBP). Land classification at 1/6° resolution for 18 surface types are  
24 converted to the ABI 2-km grid over the (CONTiguous States of the United States) (CONUS) and  
25 subsequently re-grouped to 12 IGBP types to match the classification of the CERES ADMs. In the



26 simulations, default information on aerosols and clouds is based on the ones used in MODTRAN.  
27 Comparison of derived fluxes at the TOA is made with those from the CERES and/or the Fast Longwave  
28 and Shortwave Radiative Flux (FLASHFlux) data. A satisfactory agreement between the fluxes was  
29 observed and possible reasons for differences have been identified; the agreement of the fluxes at the  
30 TOA for predominantly clear sky conditions was found to be better than for cloudy sky due to possible  
31 time shift in observation times between the two observing systems that might have affected the position  
32 of the clouds during such periods.

33

## 34 **1 Introduction**

35

36 When a new satellite is contemplated, the exact characteristics of the newly selected sensors are not fully  
37 known; simulations of proposed sensors are also not readily available. Yet, there is a need to obtain a  
38 priori information on the expected performance of the new instruments. This is usually accomplished by  
39 using characteristics of instruments in closest resemblance to the proposed ones and performing  
40 simulations that can provide insight on the expected performance of the new instrument. As such, an  
41 evolutionary process can be expected and it did precede activities reported in this manuscript.

42 The “indirect path method” used at the Center for Satellite Applications and Research (STAR) (Laszlo et  
43 al., 2020) for deriving SW radiative fluxes from satellite observations requires knowledge of the SW  
44 broadband (0.2 – 4.0  $\mu\text{m}$ ) top of the atmosphere (TOA) albedo. The Advanced Baseline Imager (ABI)  
45 observations onboard of the NOAA GOES-R series of satellites provide reflectances in six narrow bands  
46 in the shortwave spectrum (**Table 1**); these must be first transformed into broadband reflectance (the  
47 narrow-to-broadband, NTB, conversion process), and then the broadband reflectance must be transformed  
48 into a broadband albedo (the ADM conversion process).

49 During the pre-launch activity NTB transformations were developed based on theoretical radiative  
50 transfer simulations with MODTRAN-3.7 and 14 land use classifications from the International  
51 Geosphere-Biosphere Programme (*IGBP*) (Hansen et al., 2010). They were augmented with ADMs from



52 (CERES) observed ADMs (Loeb et al., 2003) and theoretical simulations (Niu and Pinker, 2011) to  
53 compute TOA fluxes. The resulting NTB transformations and ADMs have been tested using proxy data  
54 and simulated ABI data. The proxy instruments used in the simulations include the GOES-8 satellite, the  
55 Advanced Very-High Resolution Radiometer (AVHRR) sensor on the Polar Orbiting satellites, the  
56 Spinning Enhanced Visible Infra-Red Imager (SEVIRI) sensor on the European METEOSAT Second  
57 Generation (MSG) satellites, and the Moderate Resolution Imaging Spectroradiometer (MODIS)  
58 instrument on the NASA Terra and Aqua Polar Orbiting satellites (Pinker et al., 2021, unpublished). For  
59 each of these satellites, the evaluation of the methodologies was done differently; some results were  
60 evaluated against ground observations while others, against TOA information from CERES as well as  
61 from the (ESA) Geostationary Earth Radiation Budget (GERB) satellite (Harries et al., 2005). The results  
62 obtained provided an insight on the expected performance of the new ABI sensor. Those procedures have  
63 been subsequently updated and applied to the new ABI instrument once it was built and fully  
64 characterized.

65 In this paper we describe activity in support of methodologies to derive surface shortwave (SW) radiative  
66 fluxes from the operational Advanced Baseline Imager (ABI) instrument on the GOES-R series of the  
67 NOAA geostationary meteorological satellites. We describe the physical basis and the development of  
68 the (NTB) transformations of satellite observed radiances and the bi-directional corrections to be applied  
69 to the broadband reflectance to obtain broadband TOA albedo. The methodology will be presented in  
70 section 2, results in section 3 and a summary and discussion in section 4.

71

## 72 **2. Methodology**

73

74 The following two flowcharts (**Figs. 1 and 2**) describe the necessary steps to derive the NTB  
75 transformations and the ADMs. Details of these two steps will follow.



76 The TOA narrowband and broadband reflectances can be calculated from the spectral radiances  
 77 simulated from MODTRAN 4.3 and the response functions of the satellite sensor as shown in equations  
 78 (1) and (2):

$$\rho_{nb}(\theta_0, \theta, \phi) = \frac{\pi \int_{\lambda_1}^{\lambda_2} I(\lambda, \theta_0, \theta, \phi) G(\lambda) d\lambda}{\int_{\lambda_1}^{\lambda_2} \cos(\theta_0) S_0(\lambda) G(\lambda) d\lambda} \quad (1)$$

$$\rho_{bb}(\theta_0, \theta, \phi) = \frac{\pi \int_{0.2 \mu m}^{4 \mu m} I(\lambda, \theta_0, \theta, \phi) d\lambda}{\int_{0.2 \mu m}^{4 \mu m} \cos(\theta_0) S_0(\lambda) d\lambda} \quad (2)$$

81  
 82 where  $\rho_{nb}$  is narrowband reflectance;  $\rho_{bb}$  is broadband reflectance;  $\theta_0$ : solar zenith angle;  $\theta$ : view  
 83 (satellite) zenith angle;  $\phi$ : relative azimuth angle;

84  $I_\lambda$ : reflected spectral radiance;  $S_0(\lambda)$ : solar spectral irradiance;

85  $G_\lambda$ : spectral response functions of satellite sensors;  $\lambda_1$  and  $\lambda_2$  are the spectral limits of the sensor spectral  
 86 band.

87 As stated previously, the ADMs from CERES-based observations (Loeb et al., 2003) were augmented  
 88 with theoretical simulations (Niu and Pinker, 2011) to compute TOA fluxes. This due to the fact that  
 89 CERES observations at higher latitudes are under-sampled or not existent.

90 The combined ADMs are developed for each angular bin by weighting the modeled and CERES ADMs  
 91 based on the number of samples used to derive the ADMs of each type (Niu et al., 2011). Specifically:

$$\bar{R}(\theta_0, \theta, \phi) = \frac{1}{m+n} (m \times R_{CERES}(\theta_0, \theta, \phi) + n \times R_S(\theta_0, \theta, \phi)) \quad (3)$$

93  $\bar{R}(\theta_0, \theta, \phi)$ : averaged ADMs at each angular bin;



- 94  $R_{CERES}$ : anisotropic factor from CERES ADMs;  
95  $R_S$ : anisotropic factor from simulated ADMs;  
96  $m$  and  $n$ : observation numbers at angular bins for CERES and simulated ADMs.

97

98

## 99 2.1 Selection of Atmospheric profiles for simulations

100

101 We have selected 100 atmospheric profiles covering the globe and the seasons, to use as input for  
102 simulations with MODTRAN4.3. A tool was developed to select profiles from a Training Data set known  
103 as SeeBor Version 5.0 ([https://cimss.ssec.wisc.edu/training\\_data/](https://cimss.ssec.wisc.edu/training_data/)) (Borbas et.al. 2005). Originally it  
104 consisted of 15704 global profiles of temperature, moisture, and ozone at 101 pressure levels for clear  
105 sky conditions. The profiles are taken from NOAA-88, and the European Centre for Medium-Range  
106 Weather Forecasts (ECMWF) 60L training set, TIGR-3, ozone-sondes from 8 NOAA Climate Monitoring  
107 and Diagnostics Laboratory (CMDL) sites, and radiosondes from the Sahara Desert during 2004. A  
108 technique to extend the temperature, moisture, and ozone profiles above the level of existing data was  
109 also implemented by the providers (University of Wisconsin-Madison, Space Science and Engineering  
110 Center, Cooperative Institute for Meteorological Satellite Studies (CIMSS)). **Fig. 3** shows the selected  
111 profile locations; each season includes 25 profiles.

112 The SeeBor profiles are clear sky profiles. The top of the profiles is at 0.005 mb which is about 82.6 km.  
113 We did an experiment to check the impact of reducing the number of levels for a profile (initially,  
114 we have used only 40 levels). In the experiment computed were radiances from profiles with 50  
115 levels as well as radiances from profiles with 98 Levels. The difference between the two radiances  
116 (50 lev-98 lev) were below 5 % reaching 15 % around 2.5  $\mu\text{m}$ . In the experiment we used the odd  
117 number levels starting from surface (plus the highest level) to reduce the number of profile levels.  
118 Based on these experiments we have opted to keep all 98 profile levels.



119 The atmospheric profiles at each pressure level include temperature, water vapor and ozone. The surface  
120 variables include surface skin temperature, 2 m temperature, land/sea mask, and albedo. We have  
121 conducted a thorough investigation how the selected profiles represent the entire sample of 15704 profiles.  
122 An example showing the comparison of temperature, humidity and ozone profiles is shown in **Fig. 4**. As  
123 seen, there is a positive bias in the selected profiles due to their higher concentration at the lower latitudes.  
124 Since our domain of study is in such latitudes this selection should not have adverse effects on the  
125 simulations.

## 126 **2.2 Surface conditions**

127  
128 Surface condition is one of the primary inputs into the MODTRAN simulations. The International  
129 Geosphere-Biosphere Programme (IGBP) land classification is used as data source (Hansen et al., 2010;  
130 Loveland et al., 2010). The dataset is at 1/6-degree resolution and includes 18 surface types. We have  
131 converted the 1/6° (~18.5 km) resolution to the ABI 2-km grid using the nearest grid method (**Fig. 5**). The  
132 method for cloudy sky uses 4 surface types; these are also derived from 12 IGBP types (**Table 2**).

## 133 134 **2.3 Clear and cloudy sky simulations**

135  
136 Under clear sky, multiple scattering from aerosols is important. We have included 6 aerosol types (**Table**  
137 **3**) to cover a range of possible conditions under clear sky. Aerosol models are selected based on the type  
138 of extinction and a default meteorological range for the boundary-layer aerosol models as listed below:

139 Aerosol Type 1: Rural extinction, visibility = 23 km

140 Aerosol Type 4: Maritime extinction, visibility = 23 km

141 Aerosol Type 5: Urban extinction, visibility = 5 km

142 Aerosol Type 6: Tropospheric extinction, visibility = 50 km

143 Aerosol Type 8: Advective Fog extinction, visibility = 0.2 km

144 Aerosol Type 10: Desert extinction, visibility based on wind speed



145 For the 6 aerosol types, the total number of MODTRAN simulations for each surface type is 288,000.  
146 When doing NTB simulation, we use all 6 types of aerosols. The Rural, Ocean, Urban and Fog aerosols  
147 are distributed in the lower 0-2 km region. Tropospheric aerosol is distributed from 0 to 10 km tropopause.  
148 The Rural, Ocean, Urban and Tropospheric aerosol optical properties have Relative Humidity (RH)  
149 dependency. The Single Scattering Albedo (SSA) is given on 4 RH grids (0, 70, 80, 99) on a spectral grid  
150 of 788 points ranging from 0.2 to 300 microns. The Desert aerosol is wind speed dependent and the optical  
151 properties are given for 4 wind speeds (0, 10, 20, 30).  
152 Simulations were performed for ABI for all the cloud cases described in **Table 3**. To merge cloud layers  
153 with atmospheric profiles we have followed the procedure as described in *Berk et al.* (1985, 1998),  
154 namely: “Cloud profiles are merged with the other atmospheric profiles (pressure, temperature, molecular  
155 constituent, and aerosol) by combining and/or adding new layer boundaries. Any cloud layer boundary  
156 within half a meter of an atmospheric boundary layer is translated to make the layer altitudes coincide;  
157 new atmospheric layer boundaries are defined to accommodate the additional cloud layer boundaries.”  
158 100% relative humidity is assumed within the cloud layers (default).

## 160 **2.4 Selection of angles**

161  
162 The total number of angles used in the simulations is given in **Table 4**. The selected spectral grids for  
163 solar zenith angles, satellite view angles and azimuth angles are at Gaussian quadrature points, plus 0° to  
164 solar zenith angles (sza) and satellite viewing angles (vza) and 0° and 180° (forward and backward view)  
165 to the satellite relative azimuth angles. Solar angle and satellite view angle are referenced to target or  
166 surface for satellite simulation with 0° meaning looking up (zenith). Azimuth angle is defined as when  
167 the relative azimuth angle equals 180°, the sun is in front of observer.

168 The definitions of solar zenith angle and azimuth angle in this table corresponds to the definitions of  
169 MODTRAN but that is not the case for the satellite zenith angle. MODTRAN uses nadir angle as 180°-  
170 satellite zenith angle, ignoring spherical geometry.



171  
172 **2.5 Selection of optimal computational scheme**

173  
174 Computational speed is an issue for simulations that account for multiple scattering. MODTRAN4.3  
175 provides three multiple scattering models (Isaacs, DISORT, and Scaled Isaacs) and three band models at  
176 resolutions ( $1\text{ cm}^{-1}$ ,  $5\text{ cm}^{-1}$ , and  $15\text{ cm}^{-1}$ ). The DISORT model (Stamnes et al., 1988) provides the most  
177 accurate radiance simulations but the runs are very time consuming. The Isaacs (Isaacs et al. 1987) 2-  
178 stream algorithm is fast but oversimplified. The Scaled Isaacs method performs radiance calculations at  
179 a small number of atmospheric window wavelengths. The multiple scattering contributions for each  
180 method are identified and ratios of the DISORT and Isaacs methods are computed. This ratio is  
181 interpolated over the full wavelength range, and finally, applied as a multiple scattering scale factor in a  
182 spectral radiance calculation performed with the Isaacs method.

183 To optimize simulation speed and accuracy, we performed various sensitivity tests, including  
184 combinations of multiple scattering models, band resolution, and number of streams. **Table 5** lists  
185 simulation options and their corresponding calculation speed. The most computationally extensive option  
186 is DISORT 8-stream with  $1\text{ cm}^{-1}$  resolution which requires 930 seconds to finish one single run. The  
187 fastest is Scaled Isaacs with  $15\text{ cm}^{-1}$  resolution which only needs 6.67 seconds. Number of streams does  
188 not affect the Scaled Isaacs calculation speed. This is different from Isaacs and DISORT for which both  
189 stream number and band resolution have notable effects.

190 Based on results presented in **Table 5**, the efficient options ( $< 40$  seconds) are Isaacs, DISORT 2-stream  
191 with  $15\text{ cm}^{-1}$ , DISORT 4-stream  $15\text{ cm}^{-1}$ , and Scaled Isaacs all streams at all resolutions. Although the  
192 ideal option is DISORT 8-stream with  $1\text{ cm}^{-1}$  resolution, there is a trade-off between speed and accuracy.  
193 **Fig. 6** compares DISORT simulated radiances at three band resolutions. We use two spectral ranges of  
194  $0.4 - 0.5\ \mu\text{m}$  and  $1.5 - 2.0\ \mu\text{m}$  to illustrate the differences. **Fig. 6** shows that the coarser band resolution  
195 has smoothed out the radiance variations. The  $15\text{ cm}^{-1}$  has the smoothest curve among the three, and  $1$   
196  $\text{cm}^{-1}$  shows more variations than the other two. Another (scientific) criteria for selecting the spectral



197 resolution is the ability to resolve/match the relative spectral response function (SRF) of a sensor. For  
198 example, the SRFs of channels 1-6 of ABI are given at every  $1 \text{ cm}^{-1}$ .

199 Accordingly, we have chosen the  $1 \text{ cm}^{-1}$  band model for the MODTRAN radiance simulations. Performed  
200 were also radiance simulations from different multiple scattering models at  $1 \text{ cm}^{-1}$  resolution. The whole  
201 spectrum of  $0.2 - 4 \text{ }\mu\text{m}$  was separated to 14 sections so that the differences can be assessed clearly. For  
202 wavelength below  $0.3 \text{ }\mu\text{m}$  and beyond  $2.5$  no discernible differences were found among Isaacs, DISORT  
203 2-, 4-, and 8-stream, and Scaled Isaac. The largest differences occurred in the spectral range of  $0.4 - 1.0$   
204  $\mu\text{m}$ . Scaled Isaac 8-stream follows DISORT 8-stream closely across the whole spectral range; the Scaled  
205 Isaac method provided near-DISORT accuracy with the speed of Isaacs. Thus, the MODTRAN4.3  
206 simulations for GOES-R ABI were set-up with Scaled Isaac 8-stream with  $1 \text{ cm}^{-1}$  band resolution.

207 For illustration, in **Fig. 7** compared are radiances simulated by Isaac 2 stream, Scaled Isaac, and DISORT-  
208 4 stream for the case of Relative Azimuthal Angle= $1.9^\circ$ , View Angle= $76.3^\circ$ , Solar Zenith Angle= $87.2^\circ$ .  
209 The lines are differences between various settings and DISORT-8 stream (e.g. Isaacs minus DISORT-8).  
210 Isaac has the least accuracy since it is oversimplified, 4-stream showed some improvements when  
211 compared with Isaac while still has large differences for  $0.4 \text{ }\mu\text{m}$  and is still computationally demanding.  
212 Scaled Isaac provides the smallest differences between DISORT-8. **Fig. 6** (lower) zoomed in to the large  
213 difference area of  $0.3-0.35 \text{ }\mu\text{m}$  which indicates that Scaled Isaacs still provides satisfactory results.

214

## 215 **2.6 Regression methodologies**

216

217 We have derived coefficients of regression using a non-constrained and constrained least-square curve  
218 fitting methods of Matlab “stepwisefit” and “lsqnonneg”. The first one does stepwise regression by adding  
219 terms to and removing terms from a multilinear model based on their statistical significance. It may give  
220 negative coefficients that results in a negative TOA flux, which is not a physically valid result.  
221 Subsequently, we have re-derived all the coefficients with “lsqnonneg” which can solve a linear or  
222 nonlinear least-squares (data-fitting) problem and produce non-negative coefficients.



223 To ensure that information from all channels is used and avoid the complex cross-correlation  
224 problem, it was opted to generate Narrow to Broad (NTB) coefficients for each ABI channel  
225 separately (using “lsqnonneg”). These channel specific NTB coefficients are applied to each channel  
226 to convert ABI narrow-band reflectance to extended band. The final broad-band TOA reflectance is  
227 taken as the weighted sum of all 6-channel specific broad-band reflectance. The logic behind this  
228 approach is the assumption that the narrow-band reflectance from each channel is a good  
229 representative for a limited spectral region centered around the channel and the total spectral  
230 reflectance is dominated by the spectral region that contains the most solar energy.

231 To generate “separate-channel” NTB coefficients, each narrow-band ABI channel reflectance is  
232 converted to a reflectance  $\rho_{bb,i}$  separately,

$$233 \quad \rho_{bb,i}(\theta_0, \theta, \phi) = c_{0,i}(\theta_0, \theta, \phi) + c_{1,i}(\theta_0, \theta, \phi) * \rho_{nb,i}(\theta_0, \theta, \phi) \quad (4)$$

234 where  $\rho_{bb,i}$  is the band reflectance for an interval around each channel  $i$ ;  $c_{0,i}$  and  $c_{1,i}$  are regression  
235 coefficients for channel  $i$ . These regression coefficients are derived separately for various combination of  
236 surface, cloud and aerosol types; The total shortwave broad band (0.25 – 4.0 $\mu\text{m}$ ) reflectance  $\rho_{bb}^{est}$  is  
237 obtained by taking the weighted sum of all 6  $\rho_{bb,i}$  reflectance

$$238 \quad \rho_{bb}^{est}(\theta_0, \theta, \phi) = \sum_i \rho_{bb,i}(\theta_0, \theta, \phi) \frac{S_{0,i}}{S_0} \quad (5)$$

239 Here,  $S_0$  and  $S_{0,i}$  are total solar irradiance and band solar irradiance for each channel, respectively. Band  
240 edges around the six ABI channels are: 49980, 18723, 13185, 9221, 6812, 5292, 2500  $\text{cm}^{-1}$ . The  
241 corresponding band solar irradiance values are 364, 360, 287, 168, 91, 87  $\text{W m}^{-2}$ . **Fig. 8** shows the sensor  
242 response function (SRF) and locations of the six ABI channels.

243 Coefficients are generated for clear condition and 3 types of cloudy conditions. Comparison between ABI  
244 TOA flux and CERES products are shown in Figure 9. The “separate-channel” coefficients work well for  
245 predominantly clear sky. Differences are somewhat more scattered for cloudy cases. The reason may be  
246 due to the fact that the ABI observation time and CERES product time do not match perfectly since cloud  
247 condition change quickly.



248

### 249 **3.0 Data used**

250

#### 251 **3.1 Satellite data for GOES-16 and GOES17**

252

253 The GOES Imager data were downloaded from <https://www.bou.class.noaa.gov/> and the SRF from  
254 <https://ncc.nesdis.noaa.gov/GOESR/ABI.php>

255

256 \* The CODC data were not always available from CLASS and had to be obtained from NOAA/STAR  
257 temporary archives. Also, not all the required angular information needed for implementation of  
258 regressions was available online and had to be recomputed.

#### 259 **3.2 Reference data from CERES and-FLASHFlux Level2 (FLASH\_SSF) Version 3C**

260

261 Near real-time CERES fluxes and clouds in the SSF format are available within about a week of  
262 observation (Kratz et al., 2014). They do not use the most recent CERES instrument calibration and thus  
263 contains some uncertainty. Before GOES data were transferred to the Comprehensive Large Array-data  
264 Stewardship System (CLASS) system, the NOAA/STAR archive was holding new data for about a week.  
265 Therefore, the initial evaluations had to be done only with data that overlapped in time. The CERES data  
266 known as the FLASHFlux Level2 (FLASH\_SSF) were available almost in real time and did overlap with  
267 GOES. These data were downloaded from:

268 <https://ceres.larc.nasa.gov/products.php?product=FLASHFlux-Level2>

269 Due to these limitations the early comparison was done between ABI data as archived at NOAA/STAR  
270 and the FLASHFlux products. The archiving of GOES-R at the NOAA Comprehensive Large Array-data  
271 Stewardship System (CLASS) started only in 2019 however, it contains data starting from 2017. Once the  
272 CLASS archive became available, we have augmented GOES-16 cases with observations from GOES-  
273 17; only those cases will be shown in this paper.



274

### 275 **3.3 Data preparation**

276

277 The CERES FLASHFlux\_SSF data are re-gridded to match ABI spatial resolution by bi-linear  
278 interpolation method from the Earth System Modeling Framework (ESMF) package. The full description  
279 of the package can be found via <http://earthsystemmodeling.org/regrid/#overview>. The time difference  
280 between CERES FLASHFlux\_SSF and GOES-16 data must be less than  $\pm 5$  min. e.g., if the GOES-R  
281 scanning time is 18:51, then the scripts search the FLASHFLUX points between 18:46~18:56, and use  
282 the re-gridding method mentioned above to remap the FLASHFLUX to the GOES-R (2 km) domain.  
283 Several cases will be illustrated.

284 The statistics are based on all available points in overlap area. No outliers are removed. All sky, clear sky  
285 only, and cloudy only are compared for dates randomly selected. The hour was selected when both GOES-  
286 16 and GOES-17 had overlap with CERES FLASHFlux\_SSF (Aqua/Terra) data. The coefficients for  
287 GOES-17 were obtained by replacing the GOES-16 spectral response function (SRF) by the GOES-17  
288 SRF. All the regressions have been repeated for GOES-17. The GOES-17 SRF was downloaded from  
289 <https://ncc.nesdis.noaa.gov/GOESR/ABI.php>. Simultaneous evaluation for both satellites was performed.  
290 The evaluations against the CERES FLASHFlux\_SSF data is at footprint scale and covers one hour. The  
291 GOES-16 and 17 CONUS data have 5 min intervals, and there are 12 cases in one hour; this requires to  
292 test each case independently to find the best time match with CERES FLASHFlux\_SSF.

293

## 294 **4.0 Results**

295

### 296 **4.1 Comparison between ABI TOA fluxes to those from CERES and/or FLASHFlux**

297 The FLASHFLUX is in footprint format thus it is a variable in time [flux (time)].  
298 In the matching, points that fall in the  $\pm 5$  min interval of the GOES-R scanning time are used using  
299 bilinear interpolation method to get the values for GOES-R domain (e.g., if the GOES-R scanning time



300 is 18:51, then the scripts search the FLASHFLUX points between 18:46~18:56, and use bilinear  
301 interpolation method to do the remapping to GOES-R (2 km) domain). A case for 2019/12/26 (doy 360)  
302 UTC 19:36 is illustrated in **Fig. 10**.

303 The derivation and evaluation of TOA radiative fluxes as simulated for any given instrument are quite  
304 challenging. In principle, there is a need to account for all possible changes in the atmospheric and surface  
305 conditions one may encounter in the future. Yet, to know what these conditions are at the time of actual  
306 observation when there is a need to select the appropriate combination of variables from the simulations,  
307 is a formidable task. Therefore, error can be expected due to discrepancies between the actual conditions  
308 and the selected simulations and these are difficult to estimate. The approach we have selected is based  
309 on high-quality simulations using a proven and accepted radiative transfer code (MODTRAN) of known  
310 configurations and a wide range of atmospheric conditions. We have also selected the best available  
311 estimates of TOA radiative fluxes from independent sources for evaluation. However, the matching  
312 between different satellites in space and time is challenging. In selecting the cases for evaluation, we have  
313 adhered to strict criteria of time and space coincidence as described in section 3.3.

314 We have conducted several experiments to select an appropriate regression approach to the NTB  
315 transformation ensuring that non-physical results are not encountered. Based on the samples used in this  
316 study the differences found for Terra and GOES-16 were in the range of -0.5-(-12.10) for bias and 43.28-  
317 82.09 for standard deviation; for Terra and GOES-17 they were 10.81-48.17 and 70.25-109.19,  
318 respectively. For Aqua and GOES-16 they were 7.02-29.66 and 45.55-109.08 respectively while for Aqua  
319 and GOES-17 they were 0.19-26 and 53.08-94.90, respectively (all units are  $W m^{-2}$ ). The evaluation  
320 process revealed the challenges in undertaking such comparisons. Both estimates of TOA fluxes (CERES  
321 and GOES) do no account for seasonality in the land use classification; the time matching for the different  
322 satellites is important and limits the number of samples that can be used in the comparison. Based on the  
323 results of this study recommendation for future work include the need to incorporate seasonality in land  
324 use and spectral characteristic of the various surface types. Possible stratification by season in the  
325 regressions could also be explored.



326

## 327 **5.1 Causes for differences between ABI and CERES TOA fluxes**

### 328 **5.1.1 Differences in surface spectral reflectance**

329

330 In the MODTRAN simulations we use the spectral reflectance information on various surface types as  
331 provided by MODTRAN. MODTRAN version 4.3.1 contains a collection of spectral surface reflectance  
332 dataset from the Moderate Spectral Atmospheric Radiance and Transmittance (MOSART) model  
333 (Cornette et al., 1994) and others from Johns Hopkins University Spectral Library (Baldrige et al., 2009).  
334 When doing simulation, we call the built-in surface types and use the provided surface reflectance. As  
335 such, the spectral dependence of the surface reflectance used in the simulations and matched to the  
336 CERES surface types may not be compatible with the classification of CERES.

337

### 338 **5.1.2 Issues related to surface classification**

339

340 Another possible cause for differences between the TOA fluxes is the classification of surface types as  
341 originally identified by the IGBP and used in the simulations. No seasonality is incorporated in the surface  
342 type classification and the impact can be illustrated in the following case study. Simulation results for  
343 surface type 8 (open shrub) have been checked in depth. The average simulated broad-band reflectance  
344 is around 0.2. The regression residual for this surface type is reasonably small for sun angle <80 degrees,  
345 namely, the fitted broad-band reflectance is very close to the simulated broad-band reflectance. This  
346 would indicate that the regressions are performing properly. However, when we applied the regression  
347 coefficient to the GOES-16 ABI observations, the calculated TOA broad-band reflectance was around  
348 0.45, which seemed too high. To explain why the coefficient for channel 6 for “open shrub” was high we  
349 illustrate the filter function for channel 6 and spectral albedos for open shrub, desert, woody savanna and  
350 grassland in **Fig. 14**.



351 In **Fig. 15** we show the TOA fluxes for the entire domain using the original IGBP classification (open  
352 shrub) in the area of interest and subsequent replacement with a desert surface. Due to seasonal changes  
353 in surface properties, “Desert” classification may be more appropriate for the surface type at the time of  
354 the observations. This would indicate the need for introducing seasonal variability in the classification of  
355 surface types before one selects the representative NTB transformations.

356

### 357 **5.1.3 Issues related to match-up between GOES-R and CERES**

358

359 Both Terra and Aqua have sun-synchronous, near-polar circular orbits. Terra is timed to cross the equator  
360 from north to south (descending node) at approximately 10:30 am local time. Aqua is timed to cross the  
361 equator from south to north (ascending node) at approximately 1:30 pm local time. The periods for Terra  
362 and Aqua are 99 and 98 minutes, respectively. Both have 16 orbits per day. CERES on Terra and Aqua  
363 optical FOV at nadir is 16 x 32 or 20 km resolution. Terra passes CONUS during 03-06 UTC (US night  
364 time), 16-20 UTC (US day time), and Aqua passes CONUS during 07-11 UTC (US night time), 18-22  
365 UTC (US day time).

366 Both Terra and Aqua have an instantaneous FOV values at SWATH level. There is no  
367 perfect overlap, temporally or spatially with ABI data. The ABI radiance and cloud data are on a regular  
368 grid of 2\*2 km over CONUS at each hour. To use CERES data for evaluation of ABI, there is a need to  
369 perform collocation in both time and space.

370

## 371 **6.0 Summary**

372

373 Critical elements of an inference scheme for TOA radiative flux estimates from satellite observations are:  
374 1) transformation of narrowband quantities into broadband ones;  
375 2) transformation of bi-directional reflectance into albedo by applying Angular Distribution Models  
376 (ADMs). In principle, the order in which these transformations are executed is arbitrary. However, since



377 well established, observation-based broadband ADMs derived from the Clouds and the Earth's Radiant  
378 Energy System (CERES) project already exist, the logical procedure is to do the NTB transformation on  
379 the radiances first, and then apply the ADM. This is the sequence that has been followed here. While the  
380 road map to accomplish above objectives seems well defined, reaching the final goal of having a stable  
381 up-to-date procedure for deriving TOA radiative fluxes from a new instrument like the ABI on the new  
382 generation of GOES satellites is quite complicated. The process of preparing for the usefulness of a new  
383 satellite sensor needs to be done in advance, the final configuration of the instrument becomes known at  
384 a much later stage. As such, the evaluation of the new algorithms is in a fluid stage for a long time.  
385 Agreement or disagreement with know "ground truth" is not fully informative on the performance of the  
386 new algorithms to estimate desired geophysical parameters. Additional complication is related to the lack  
387 of maturity of basic information needed in the implementation process, such as a reliable cloud screened  
388 product which in itself is in a process of development and modifications. The "ground truth", namely, the  
389 CERES observations are also undergoing adjustments and recalibration. As such, the process of deriving  
390 best possible estimates of TOA radiative fluxes from ABI underwent numerous iterations to reach its  
391 current status. An effort was made to deal the best way possible with the fluid situation. All the evaluations  
392 against CERES were repeated once the ABI data reached stability and were archived in CLASS and we  
393 used the most recent auxiliary information. The prominence of certain issues surfaced from this study  
394 itself. One example is the sensitivity to land classification which currently is static. Another issue is  
395 related to the representation of real time aerosol optical depth which is important under clear sky  
396 conditions. It is believed that only now when NOAA/STAR has a stable aerosol retrieval algorithm, it  
397 would be timely to address the aerosol issue in the estimation of TOA fluxes under clear sky.  
398



399 Data availability. The data are available upon request from the corresponding author.

400 Author contributions. The investigation and conceptualization were carried out by RTP, IL and JD. YM  
401 and WC developed the software. RTP prepared the original draft. All authors contributed to the writing,  
402 editing and review of the publication.

403 Competing interests. The authors declare that they have no conflict of interest.

404 Disclaimer. Publisher's note: Copernicus Publications remains neutral with regard to jurisdictional claims  
405 in published maps and institutional affiliations.

406 Acknowledgements. We acknowledge the benefit from the use of the numerous data sources used in this  
407 study. These include the Clouds and the Earth's Radiant Energy System (CERES) teams, the Fast  
408 Longwave and Shortwave Radiative Flux (FLASHFlux) teams, the  
409 University of Wisconsin-Madison, Space Science and Engineering Center, Cooperative Institute for  
410 Meteorological Satellite Studies (CIMSS) for providing the SeeBor Version 5.0 data  
411 ([https://cimss.ssec.wisc.edu/training\\_data/](https://cimss.ssec.wisc.edu/training_data/)), and the final versions of the GOES Imager data were  
412 downloaded from <https://www.bou.class.noaa.gov/>. Several individuals have been involved in the early  
413 stages of the project whose contribution led to the refinements of the methodologies. These include M.  
414 M. Woncsick and Shuyan Liu.

415

416 Financial support. This research was supported by NOAA/NESDIS GOES-R Program under grants  
417 [5275562 1RPRP\\_DASR](#) and [275562 RPRP\\_DASR\\_20](#) to the University of Maryland.

418

419



420 **Reference:**

- 421 Berk, A., L. W. Bernstein, and D. C. Robertson: MODTRAN: A moderate resolution model for  
422 LOWTRAN 7, Philips Laboratory, Report AFGL-TR-83-0187, 1985, Hanscom AFB, MA.
- 423 Berk, A., G. P. Anderson, P. K. Acharya, D. C. Robertson, J. H. Chetwynd, S. M. Adler-Golden:  
424 MODTRAN Cloud and Multiple Scattering Upgrades with Application to AVIRIS, Remote Sensing  
425 of Environment, 65 (3), 367-375, [https://doi.org/10.1016/S0034-4257\(98\)00045-5](https://doi.org/10.1016/S0034-4257(98)00045-5), 1998.
- 426 Baldridge, A. M., S J. Hook, C. I. Grove, G. Rivera: The ASTER spectral library version 2, Remote  
427 Sensing of Environment 113, doi: 10.1016/j.rse.2008.11.007, 2009.
- 428 Borbas, E. E., S. Wetzel Seemann, H.-L Huang, J. Li, and W. P. Menzel: Global profile training database  
429 for satellite regression retrievals with estimates of skin temperature and emissivity. Proceedings of  
430 the XIV, International ATOVS Study Conference, Beijing, China, University of Wisconsin-  
431 Madison, Space Science and Engineering Center, Cooperative Institute for Meteorological Satellite  
432 Studies (CIMSS), Madison, WI, pp.763-770, 2005.
- 433 Clerbaux, N., J. E. Russell, S. Dewitte, C. Bertrand, D. Caprion, B. De Paepe, L. Gonzalez Sotelino, A.  
434 Ipe, R. Bantges, and H. E. Brindley: Comparison of GERB instantaneous radiance and flux  
435 products with CERES Edition-2 data, Rem. Sens. of Environ., **113**, 102-114. doi:  
436 10.1016/j.rse.2008.08.016, 2009.
- 437 Cornette, W. M., P. K. Acharya, D. C. Robertson, and G. P. Anderson: Moderate Spectral Atmospheric  
438 Radiance and Transmittance Code (*MOSART*), Rep. R-057-94 (11–30), La Jolla, CA: Photon  
439 Research Associates, 1994.
- 440 Kratz, D. P., P. W. Stackhouse Jr., S. K. Gupta, A. C. Wilber, P. Sawaengphokhai, and G. R. McGarragh4:  
441 The Fast Longwave and Shortwave Flux (FLASHFlux) Data Product: Single-Scanner Footprint  
442 Fluxes, J. Appl. Meteor. Climatol., 53, 1059-1079, doi: 10.1175/JAMC-D-13-061.1, 2014.
- 443 Hansen, M. C., R. S. Defries, J. R. G. Townshend and R. Sohlberg: Global land cover classification at  
444 1km spatial resolution using a classification tree approach, International Journal of Remote  
445 Sensing, 21(6-7):1331 – 1364, DOI:10.1080/014311600210209



- 446 <https://doi.org/10.1080/014311600210209>, 2010.
- 447 Harries, J. E., J. E. Russell, J. A. Hanafin, H. Brindley, J. Futyan, J. Rufus, S. Kellock, G. Matthews, R.  
448 Wrigley, A. Last, J. Mueller, R. Mossavati, J. Ashmall, E. Sawyer, D. Parker, M. Caldwell, P M.  
449 Allan, A. Smith, M. J. Bates, B. Coan, B. C. Stewart, D. R. Lepine, L. A. Cornwall, D. R. Corney,  
450 M. J. Ricketts, D. Drummond, D. Smart, R. Cutler, S. Dewitte, N. Clerbaux, L. Gonzalez, A.  
451 Ipe, C. Bertrand, A. Joukoff, D. Crommelynck, N. Nelms, D. T. Llewellyn-Jones, G. Butcher, G.  
452 L. Smith, Z. P Szewczyk, P E. Mlynczak, A. Slingo, R. P. Allan, and M. A. Ringer: The  
453 Geostationary Earth Radiation Budget Project, Bull. Amer. Meteor. Soc. 86 (7): 945, doi:  
454 10.1175/BAMS-86-7-945, 2005.
- 455 Isaacs, R. G., W.-C. Wang, R. D. Worsham, and S. Goldenberg, S.: Multiple scattering LOWTRAN and  
456 FASCODE models. Applied Optics, 26(7), 1272 – 1281, 1987.
- 457 Laszlo, I., H. Liu, H. -Y. Kim, and R. T. Pinker: GOES-R Advanced Baseline Imager (ABI) Algorithm  
458 Theoretical Basis Document (ATBD) for Downward Shortwave Radiation (Surface), and Reflected  
459 Shortwave Radiation (TOA), version 3.1, Available at <https://www.goes-r.gov/resources/docs.html>,  
460 2018.
- 461 Laszlo, I., H. Liu, H.-Y. Kim, and R. T. Pinker: Shortwave Radiation from ABI on the GOES-R Series,  
462 in *The GOES-R Series*, edited by S. J. Goodman, T. J. Schmit, J. Daniels and R. J. Redmon, pp. 179-  
463 191, Elsevier, doi: <https://doi.org/10.1016/B978-0-12-814327-8.00015-9>, 2020.
- 464 Loeb, N. G., N. M. Smith, S. Kato, W. F. Miller, S. K. Gupta, P. Minnis, and B. A. Wielicki: Angular  
465 Distribution Models for Top-of Atmosphere Radiative Flux Estimation from the Mission Satellite,  
466 Part I: Methodology, Journal of Applied Meteorology, 42 240-265, 2003.
- 467 Loveland T. R., B. C. Reed, J. F. Brown, D. O. Ohlen, Z. Zhu, L. Yang, J. W. Merchant: Development  
468 of a global land cover characteristics database and IGBP DISCover from 1 km AVHRR data,  
469 International Journal of Remote Sensing, 21 (6-7), 1303-1330, 2010.
- 470 Niu, X. and Rachel T. Pinker: Revisiting satellite radiative flux computations at the top



471 of the atmosphere, International Journal of Remote Sensing, DOI:10.1080/01431161.2011.571298,  
472 2011.

473 Stamnes, K., S.-C. Tsay, W. Wiscombe and K. Jayaweera: Numerically stable algorithm for discrete-  
474 ordinate-method radiative transfer in multiple scattering and emitting layered media, Applied  
475 Optics, 27 (12), 2502–2509, 1988.

476

477



## Tables

Table 1. Relevant information for the derivation of SW fluxes from selected satellites:  
channel information and spectral bands for ABI.

<i>ABI Band #</i>	<i>Channel</i>	<i>Spectral band (<math>\mu\text{m}</math>)</i>
1	VIS 0.47	0.45-0.49
2	VIS 0.64	0.60-0.68
3	VIS 0.86	0.847-0.882
4	NIR 1.38	1.366-1.380
5	NIR 1.61	1.59-1.63
6	NIR 2.26	2.22-2.27

478

479

480



481

482 Table 2. Surface classification description for IGBP 18 types, IGBP 12 types, CERES clear sky 6

483 types, and NTB cloudy sky 4 types

IGBP (18 types)	IGBP (12 types)	CERES clear-sky (6 types)	NTB cloudy-sky (4 types)
Evergreen Needleleaf	Needleleaf Forest	Mod-High Tree/Shrub	Land
Evergreen Broadleaf	Broadleaf Forest		
Deciduous Needleleaf	Needleleaf Forest		
Deciduous Broadleaf	Broadleaf Forest		
Mixed Forest	Mixed Forest		
Closed Shrublands	Closed Shrub		
Open Shrublands	Open Shrub	Dark Desert	
Woody Savannas	Woody Savannas	Mod-High Tree/Shrub	
Savannas	Savannas	Low-Mod Tree/Shrub	
Grasslands	Grasslands		
Permanent Wetlands			
Croplands	Croplands		
Urban and Built-up	Open Shrub	Dark Desert	Desert
Cropland Mosaics	Croplands	Low-Mod Tree/Shrub	Land
Snow and Ice	Snow and Ice	Snow and Ice	Snow and Ice
Bare Soil and Rocks	Barren and Desert	Bright Desert	Desert
Water Bodies	Ocean	Ocean	Water
Tundra	Grasslands	Low-Mod Tree/Shrub	Land

484



485

486

487 Table 3. The various classes for which NTB coefficients are generated.

Parameter	Clear condition	Cloudy condition
Aerosol or cloud type	6 aerosol types (rural, maritime, urban, tropospheric, fog, desert)	3 cloud types (cirrus, stratocumulus, altostratus)
Optical depth (OD)	Typical VIS (km) values for each aerosol types (no OD grid for each aerosol type). Rural: 23, maritime: 23, urban: 5, tropospheric: 50, fog: 0.2, desert: (default VIS for wind speed 10m/s)	Cirrus: [0, 0.8, 1.2, 1.8, 3.2] Stratocumulus: [0, 0.8, 1.2, 1.8, 3.2, 5.8, 8.2, 15.8, 32.2, 51.8, 124.2] Altostratus: [0, 15.0, 30.0, 50.0, 80.0]
Surface type	12 IGBP surface types	4 types (Water, Land, Desert, Snow/Ice)

488

489

490



491

492

493

494

Table 4. Angles used in simulations. To be consistent with what is presented in the  
ABI Shortwave Radiation Budget (SRB) Algorithm Theoretical Basis Documents (ATBD) (Laszlo  
et al, 2018) the additional angles used in the simulations are not given in this Table.

Angle Type	Angles
Solar Zenith Angle [°]	0.0, 12.9, 30.8, 41.2, 48.3, 56.5, 63.2, 69.5, 75.5, 81.4, 87.2
Satellite Zenith Angle [°]	0.0, 11.4, 26.1, 40.3, 53.8, 65.9, 76.3
Azimuth Angle [°]	0.0, 1.9, 10.0, 24.2, 44.0, 68.8, 97.6, 129.3, 162.9, 180

495

496

497



498

499

Table 5. MODTRAN simulation speed test (CPU MHz 2099.929).

Algorithm	Stream	Band Resolution (cm <sup>-1</sup> )	Speed (~seconds)
Isaacs	2	1	40
DISORT	2	1, 5, 15	280, 70, 30
	4	1, 5, 15	560, 120, 40
	8	1, 5, 15	930, 300, 110
Scaled Isaac	2	1, 5, 15	30, 10, 6.67
	4	1, 5, 15	30, 10, 6.67
	8	1, 5, 15	30, 10, 6.67

500

501

502



503

504 Table 6. Details on data used as input for calculations.

505

Short Name	Long Name	MODE	ABI-Channel	Scan Sector	Spatial Resolution
RadC	L1b Radiance	M6	C01-C06	CONUS	5000x3000
AODC	L2 Aerosol	M6	--	CONUS	2500x1500
ACMC	L2 Clear Sky Masks	M6	--	CONUS	2500x1500
ACTPC	L2 Cloud Top Phase	M6	--	CONUS	2500x1500
CODC*	L2 Cloud Optical Depth	M6	--	CONUS	2500x1500

506

507

508



509

510 Table 7. Statistical summary for all selected cases intercompared at instantaneous time  
 511 scale.

Case	CERES	GOES- R	Corr	Bias	Std	RMSE	N
09/13 2019	Terra	G16	0.87	-12.10	82.09	82.98	0.13x10 <sup>6</sup>
		G17	0.71	48.17	108.19	118.42	1.73x10 <sup>6</sup>
UTC 20	Aqua	G16	0.76	17.38	109.08	110.45	1.46x10 <sup>6</sup>
		G17	0.73	26.00	81.96	85.98	0.53x10 <sup>6</sup>
09/21 2019	Terra	G16	0.85	6.78	66.66	67.00	0.35x10 <sup>6</sup>
		G17	0.83	26.41	87.64	91.57	1.75x10 <sup>6</sup>
UTC 19	Aqua	G16	0.82	29.66	105.09	109.20	1.67x10 <sup>6</sup>
		G17	0.76	6.03	94.70	94.89	0.15x10 <sup>6</sup>
09/30 2019	Terra	G16	0.88	4.49	64.79	64.94	0.40x10 <sup>6</sup>
		G17	0.80	19.35	86.41	88.55	1.74x10 <sup>6</sup>
UTC 19	Aqua	G16	0.81	19.99	99.98	101.96	1.67x10 <sup>6</sup>
		G17	0.70	1.22	94.90	94.91	0.12x10 <sup>6</sup>
10/23 2019	Terra	G16	0.86	5.84	51.44	51.77	0.35x10 <sup>6</sup>
		G17	0.87	22.47	70.25	73.76	1.75x10 <sup>6</sup>
	Aqua	G16	0.89	17.10	75.95	77.85	1.67x10 <sup>6</sup>



UTC							
19		G17	0.78	8.98	72.52	73.07	0.15x10 <sup>6</sup>
11/08	Terra	G16	0.87	-0.5	43.28	43.28	0.35x10 <sup>6</sup>
2019		G17	0.82	17.18	71.27	73.31	1.75x10 <sup>6</sup>
UTC	Aqua	G16	0.90	10.08	71.27	71.98	1.67x10 <sup>6</sup>
19		G17	0.68	1.53	47.55	47.58	0.15x10 <sup>6</sup>
11/24	Terra	G16	0.79	7.98	49.10	49.75	0.35x10 <sup>6</sup>
2019		G17	0.87	14.10	78.35	79.61	1.76x10 <sup>6</sup>
UTC	Aqua	G16	0.82	7.63	58.68	59.17	1.67x10 <sup>6</sup>
19		G17	0.65	0.19	63.14	63.14	0.15x10 <sup>6</sup>
12/26	Terra	G16	0.89	7.6	52.79	53.33	0.35x10 <sup>6</sup>
2019		G17	0.77	10.81	73.14	73.93	1.76x10 <sup>6</sup>
UTC 19	Aqua	G16	0.83	7.02	59.16	59.58	1.67x10 <sup>6</sup>
		G17	0.73	-1.09	53.08	53.09	0.15x10 <sup>6</sup>

512

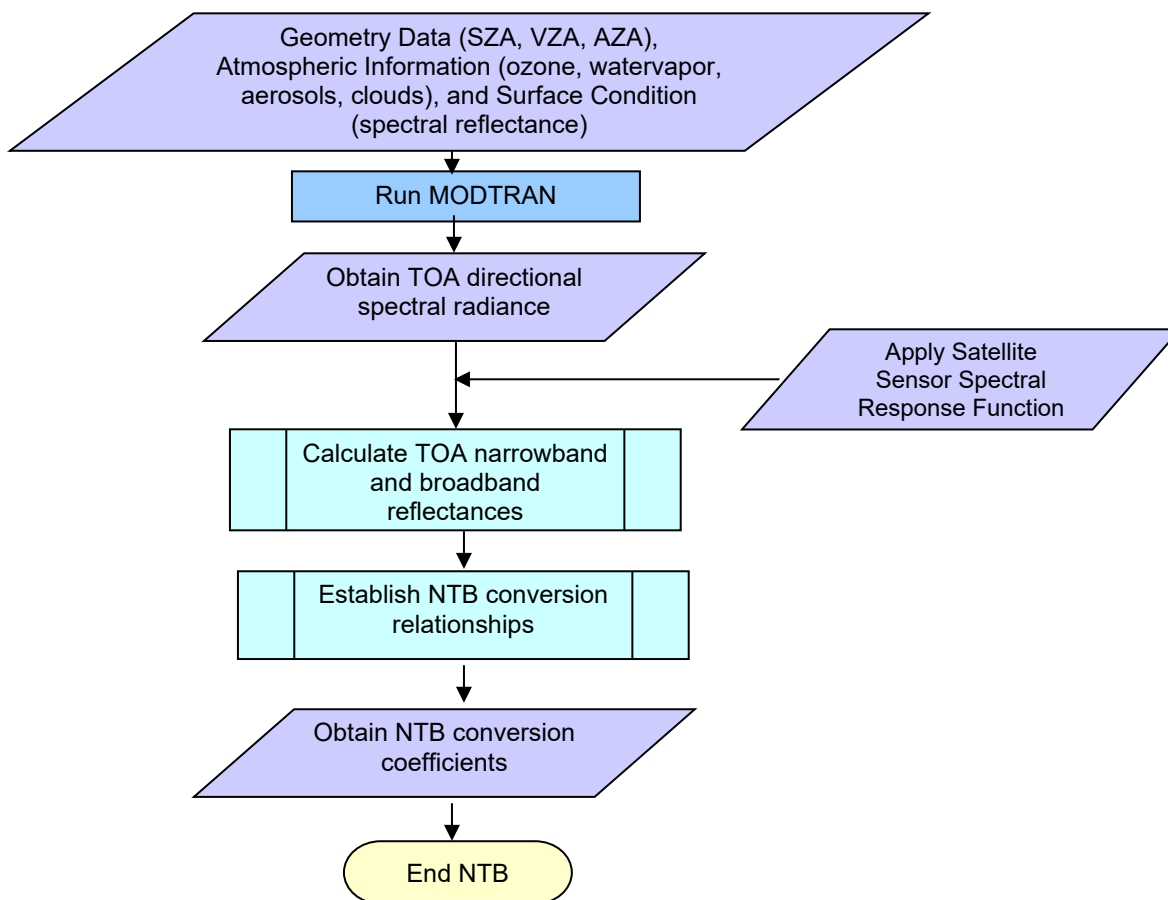
513

514



515 **Figures**

516



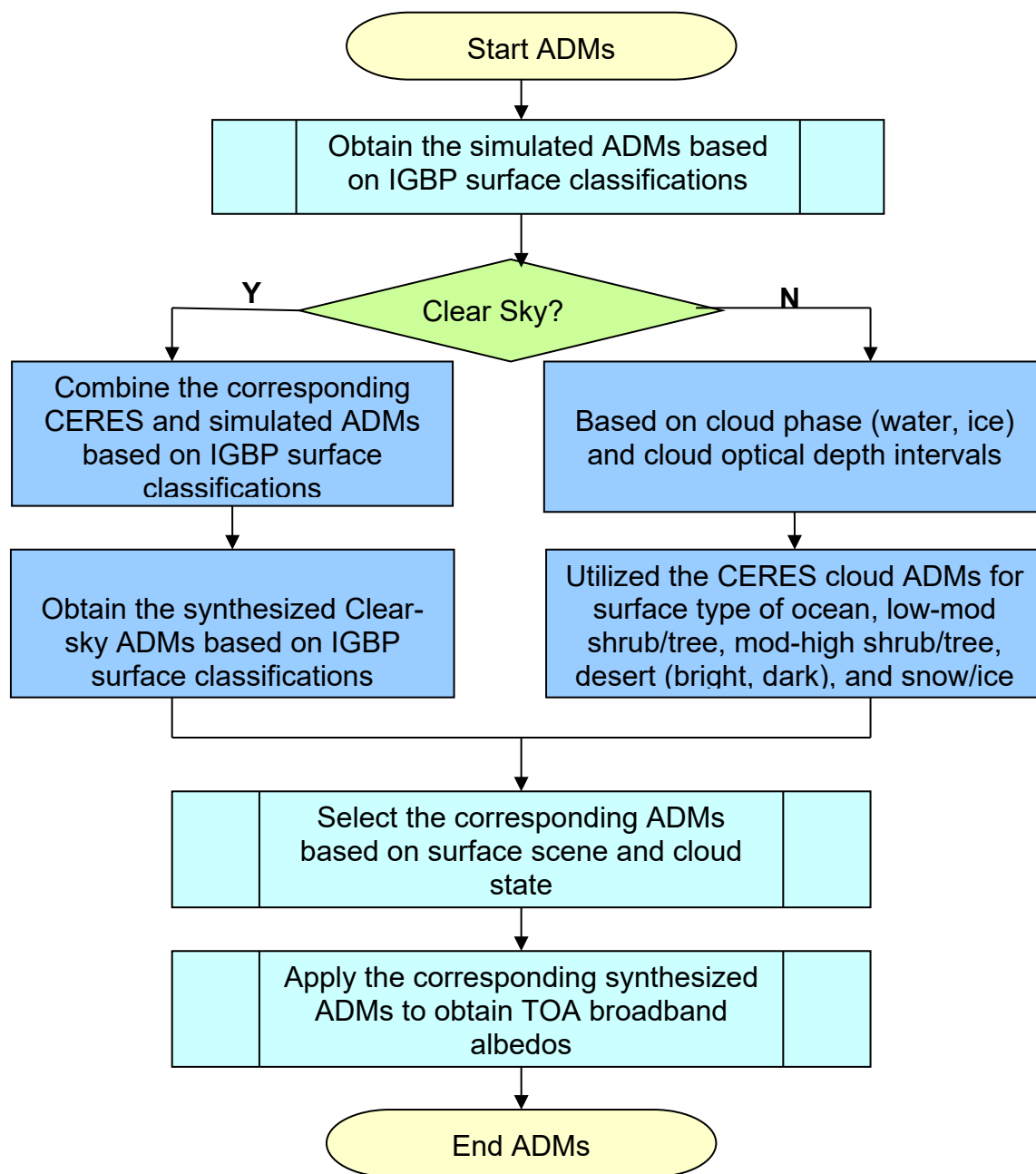
517

518 Figure 1. Flowchart of the NTB transformations illustrating the main processing sections.

519

520

521



522

523 Figure 2. Schematic illustration of the logic employed to synthesize modeled and observed ADMs.

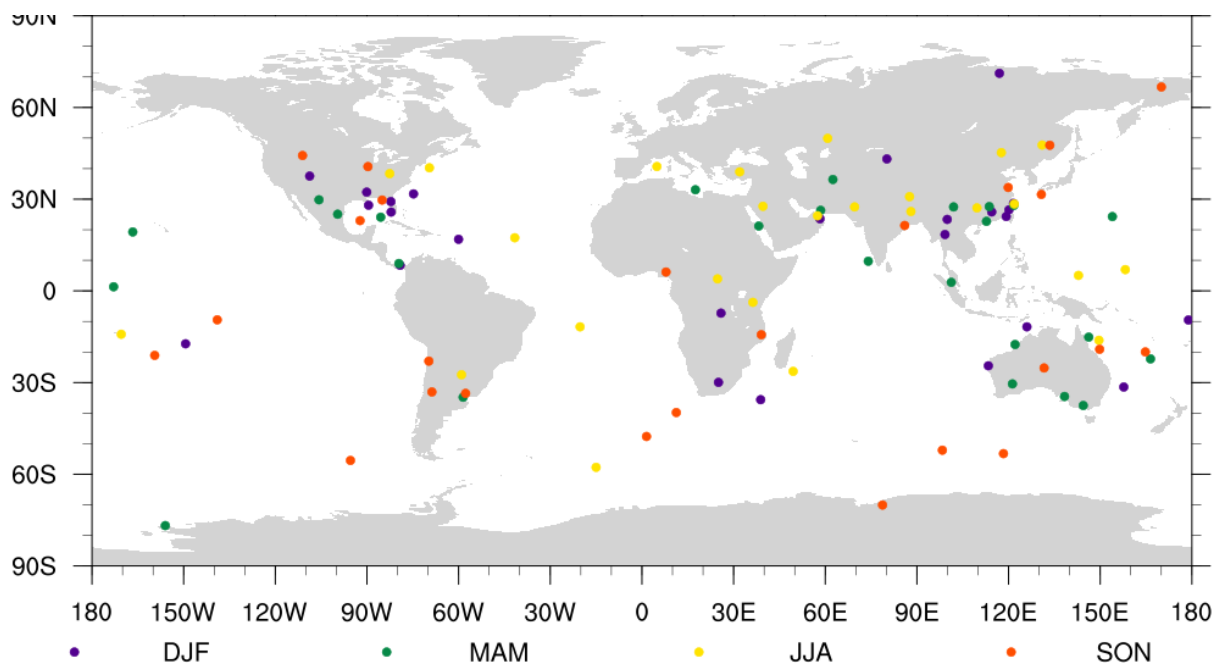


524

525

526

527

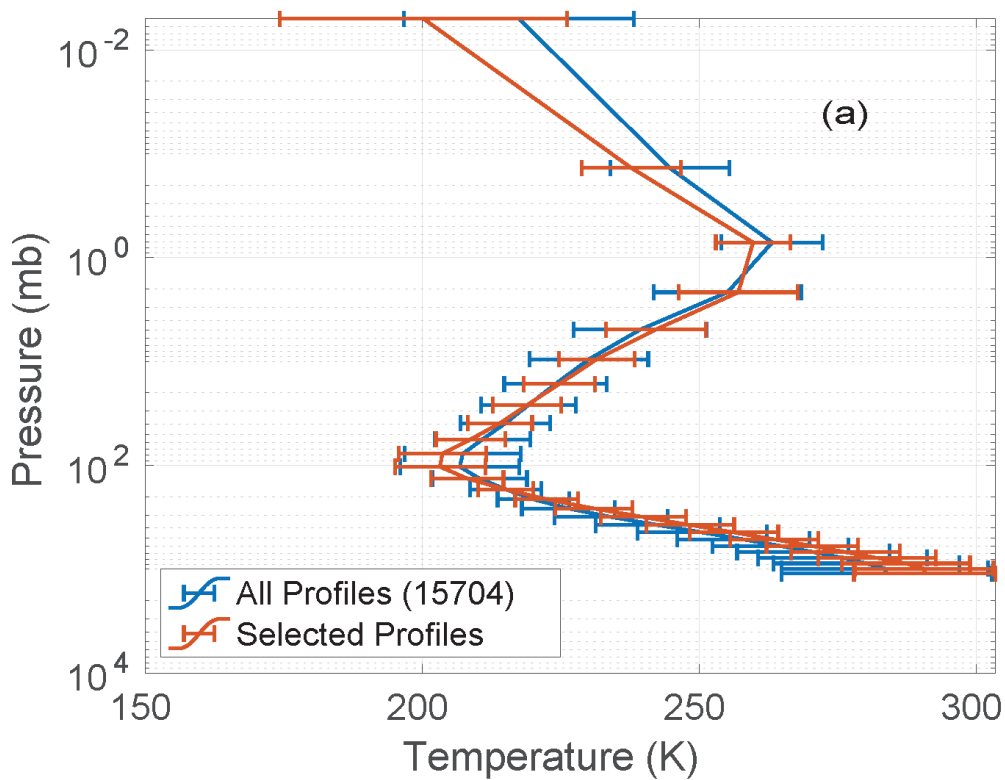


528

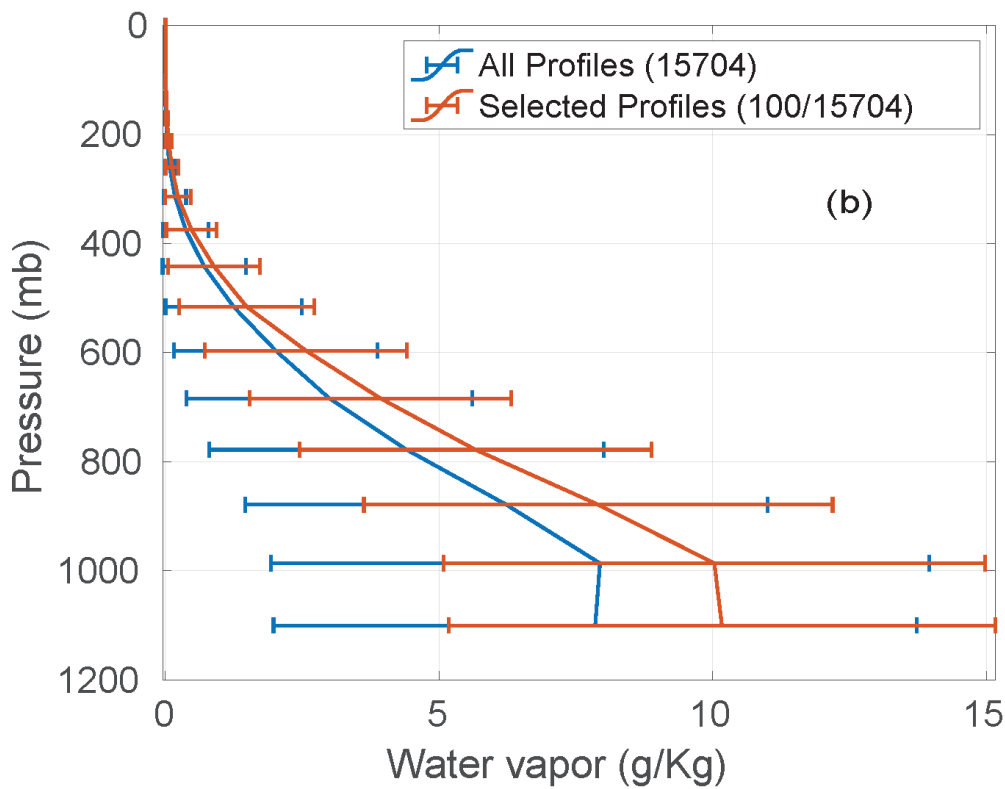
529 Figure 3. The location of the 100 selected clear sky profiles from SeeBor used in

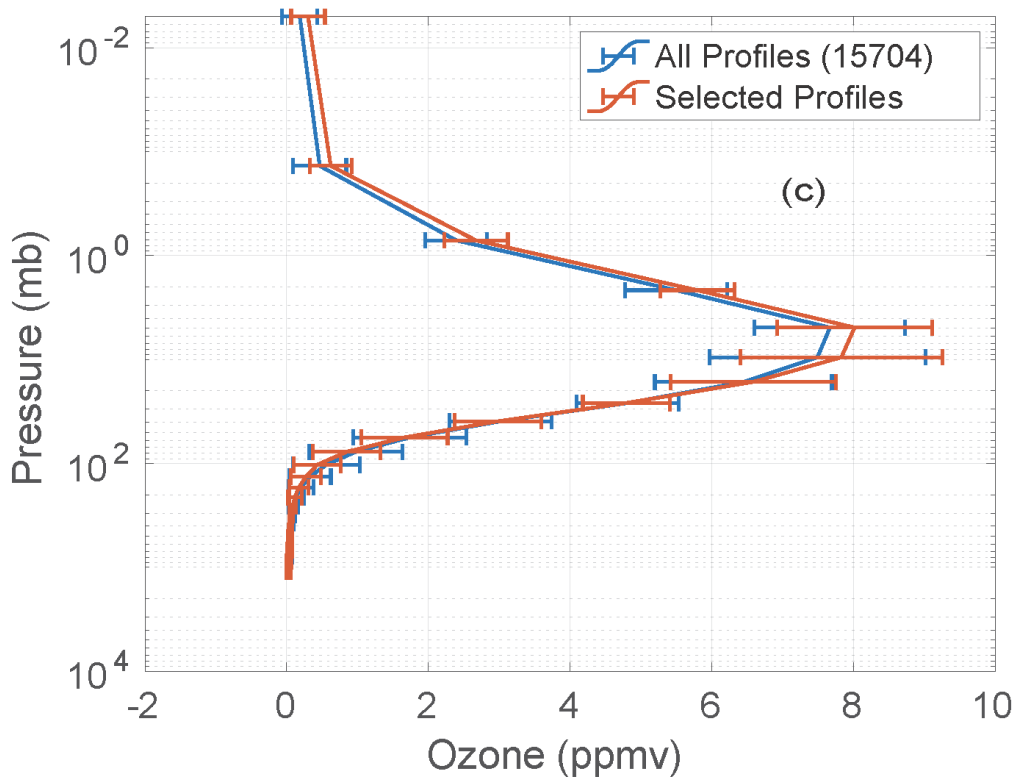
530

531



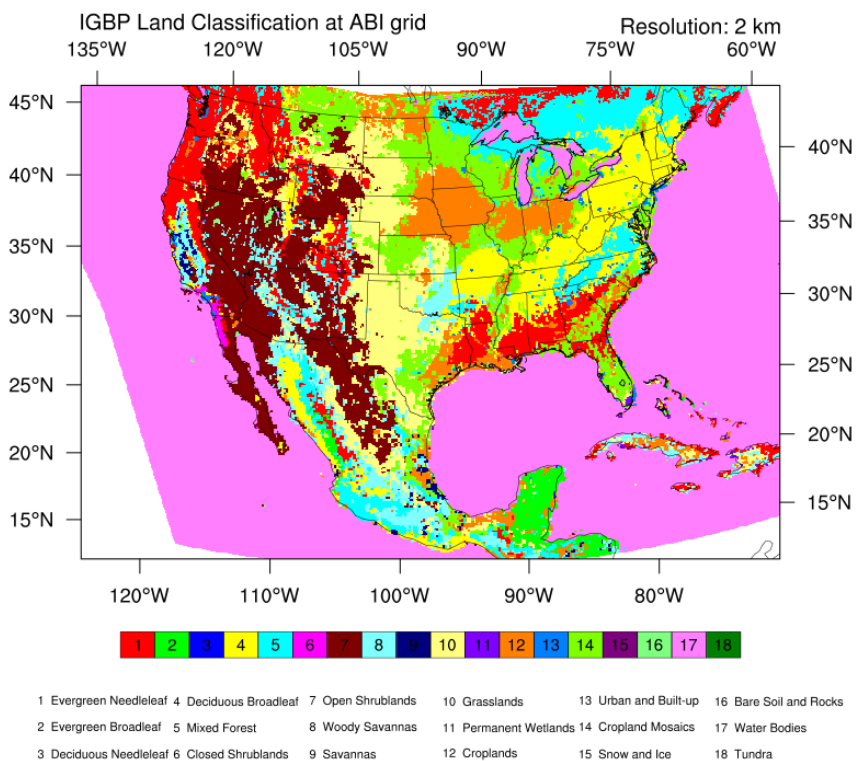
532





534  
535  
536  
537  
538  
539

Figure 4. Profile statistics of: (a) temperature; (b): water vapor; (c) ozone the entire available sample and the reduced sample used in this study. Error bar is 1 standard deviation (logarithmic scale).



540

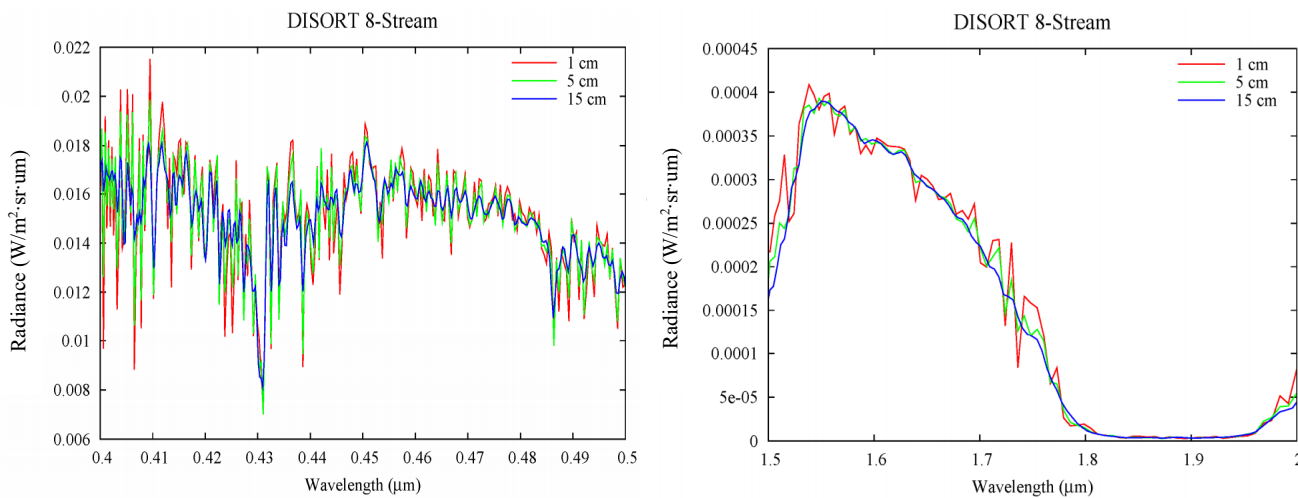
541 Figure 5. Re-mapped IGBP surface classifications over the CONUS at 2-km ABI grid.

542

543



544



545

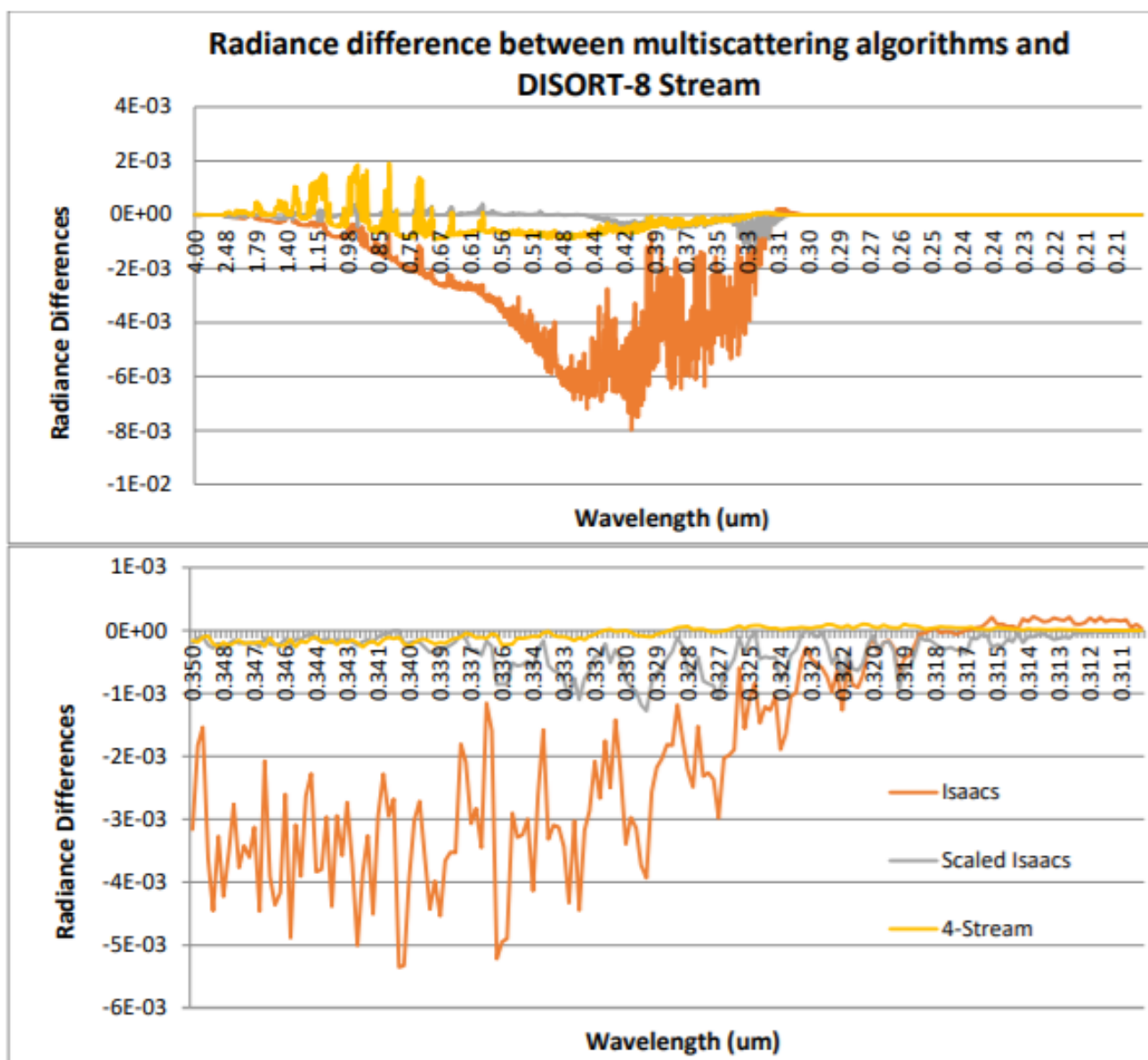
546

547

548

549

Figure 6. Simulated Radiances from DISORT 8-stream (with 1, 5, and 15  $\text{cm}^{-1}$  resolution band model for spectral range of 0.4 – 0.5  $\mu\text{m}$  (left) and 1.5 – 2.0  $\mu\text{m}$  (right).

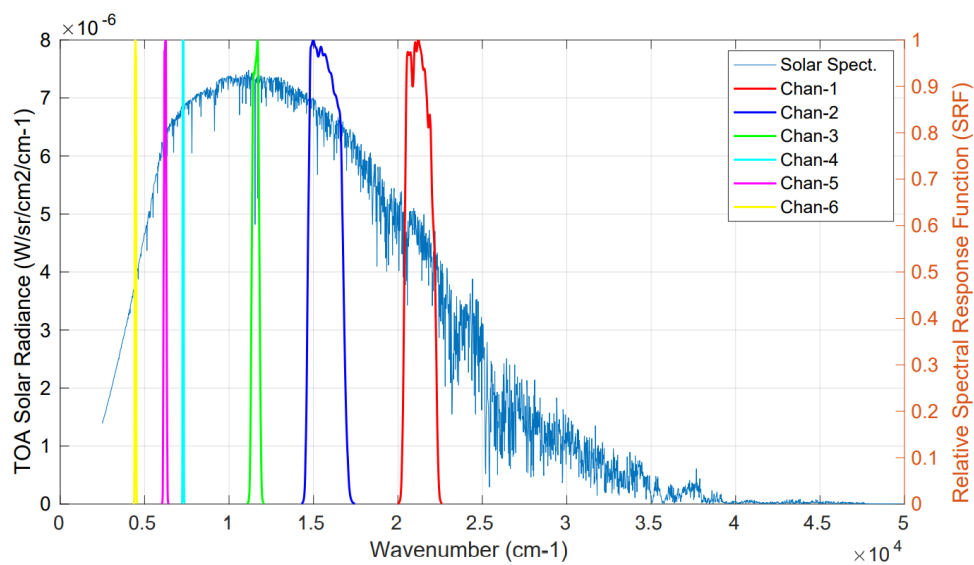


550  
551 Figure 7. Radiance differences between various multi-scattering algorithms and DISORT-8 stream.  
552 *Upper*: the whole simulated spectrum of 0.2-4  $\mu\text{m}$ ; *Lower*: zoom on 0.3-0.35  $\mu\text{m}$  (Relative Azimuthal  
553 Angle=1.9°, View Angle=76.3°, Solar Zenith Angle=87.2°).



554

555



556

557 **Figure 8.** Locations of the six ABI channel SRFs. X-axis is wavenumber. Y-axis is solar irradiance.

558

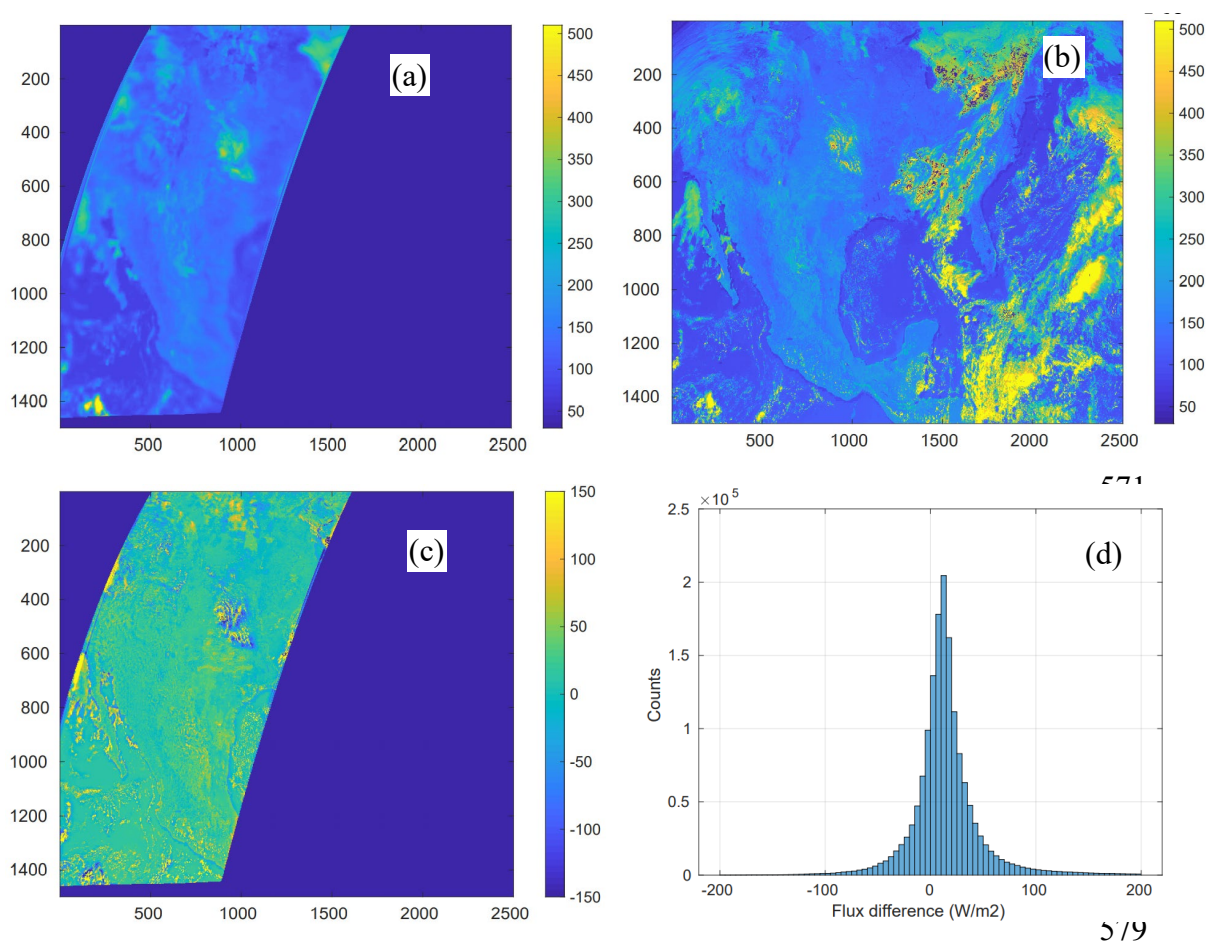
559

560



561

562



580 **Figure 9.** Comparison of TOA flux from ABI and CERES based FLASHFlux for 2017/11/25, 17:57Z.

581 (a) CERES Terra product; (b): results with “separate-channel” coefficients. (c): difference (ABI-

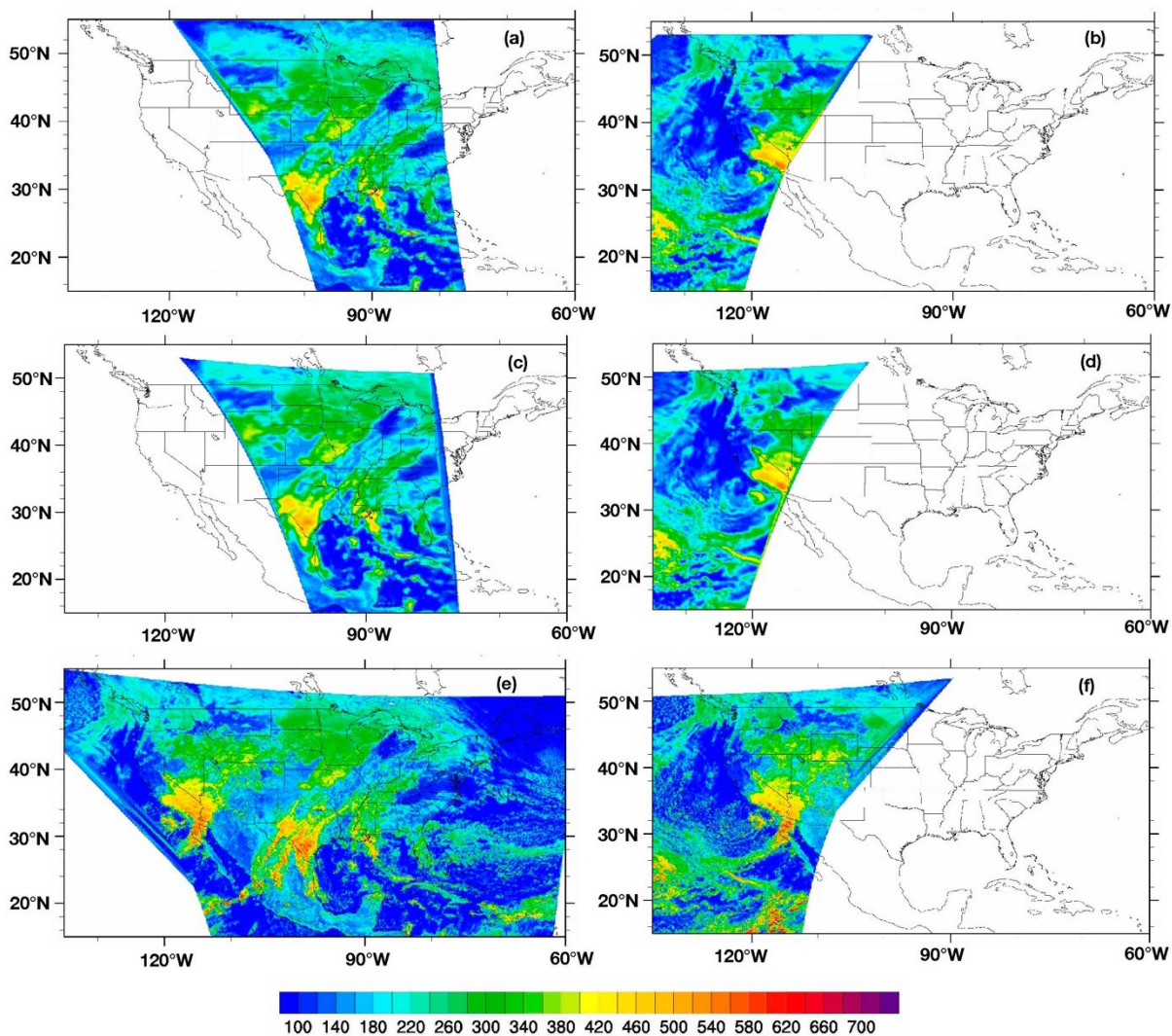
582 CERES); (d): histogram of ABI-CERES differences.

583

584



585

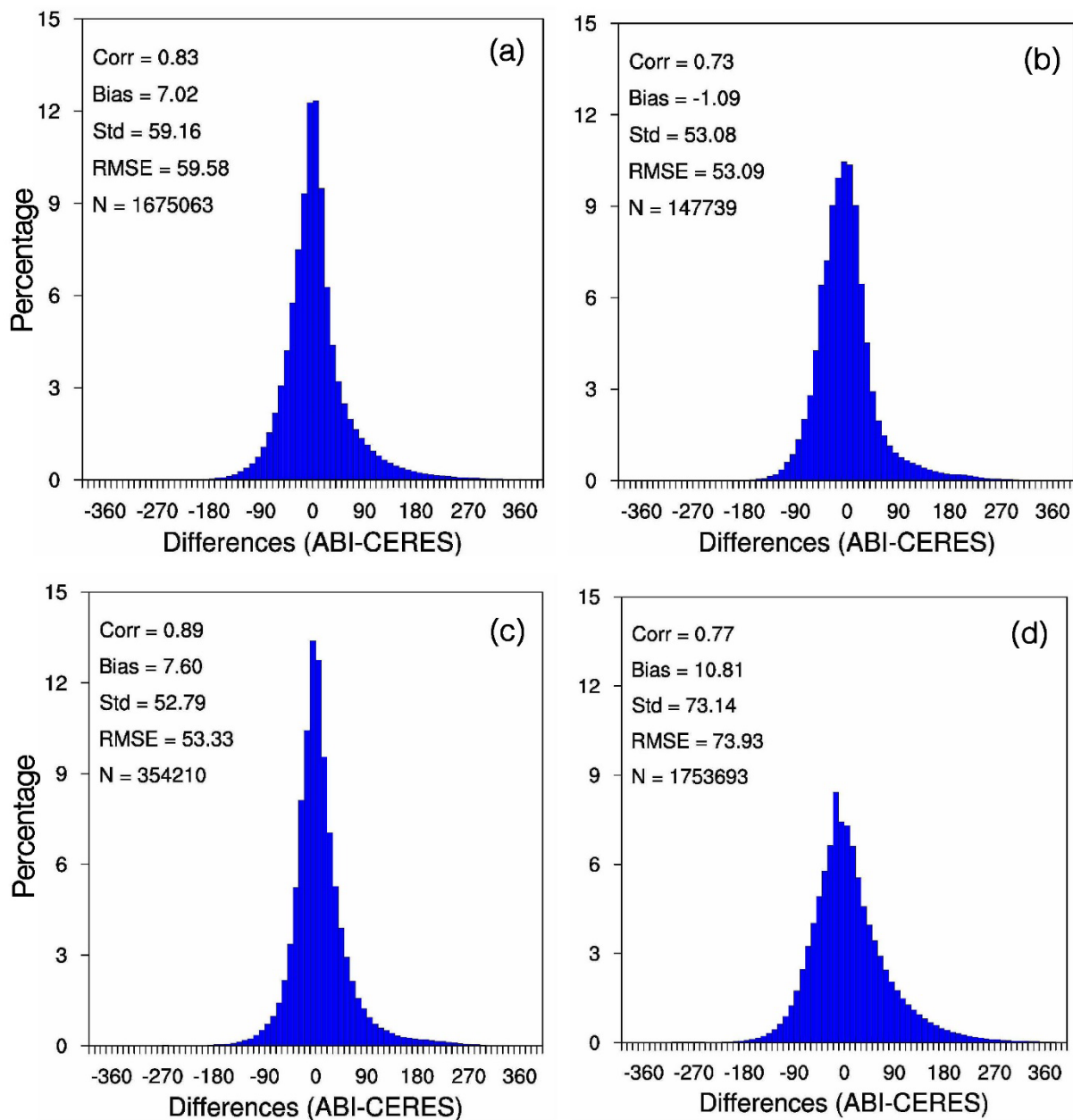


586

587 Figure 10. All sky TOA SW from CERES FLASHFlux/Aqua (a), CERES FLASHFlux/Terra (b),  
588 re-gridded CERES FLASHFlux/Aqua (c), CERES FLASHFlux/Terra GOES-16 (d) and GOES-17 (f) on  
589 12/26/2019 at UTC 19:36.

590

591

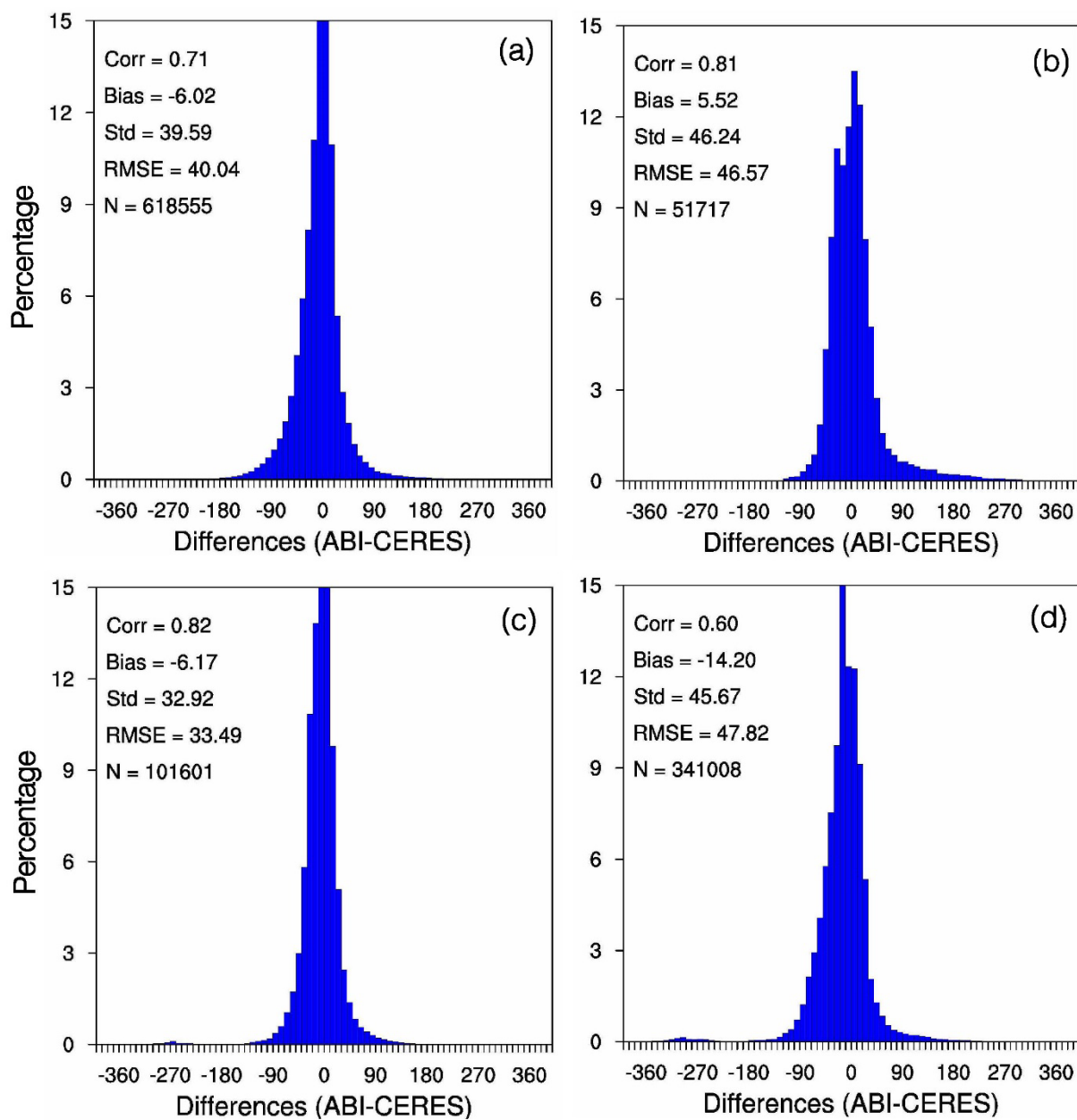


592

593 Figure 11. Frequency distribution of all-sky TOA SW differences between ABI on GOES-16 and CERES  
594 (Left) and ABI on GOES-17 and CERES (Right) using Aqua (Upper) and Terra (Lower). All observations  
595 were used (clear and cloudy) on 12/26/2019 at UTC 19:36.

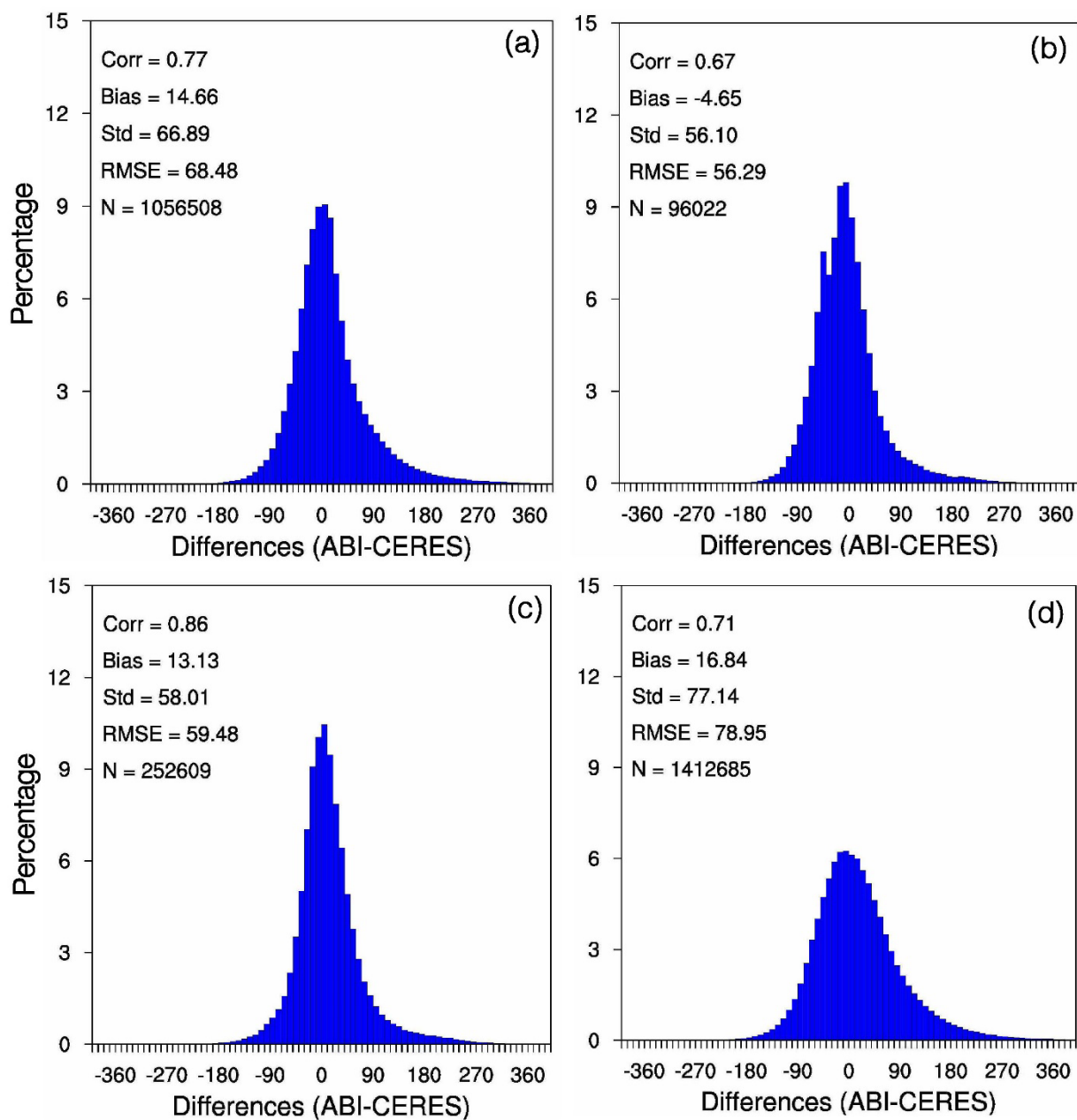


596



597

598 Figure 12. Same as Figure 11 but for clear TOA SW differences.



599

600 Figure 13. Same as Figure 11 but for cloudy TOA SW differences.

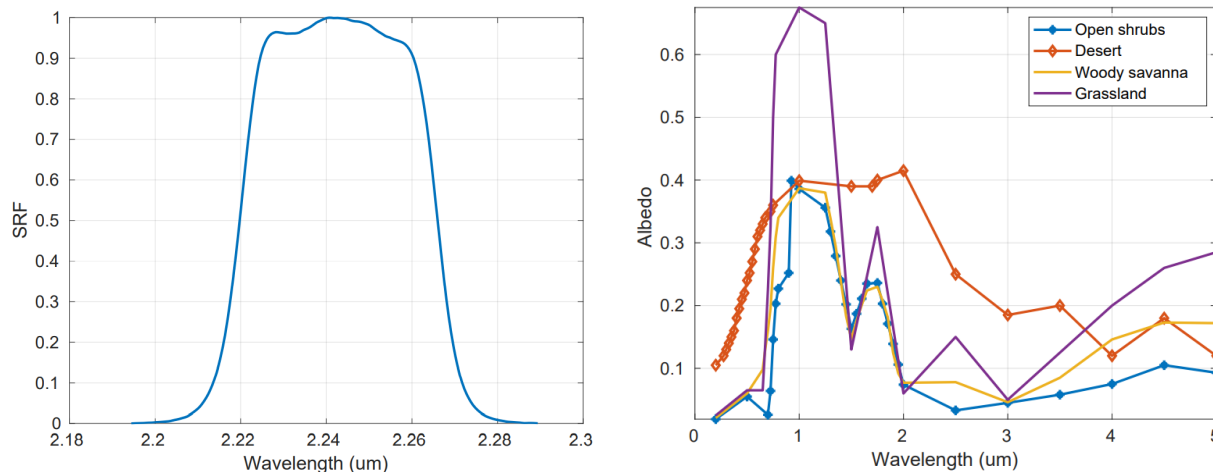
601

602



603

604



605

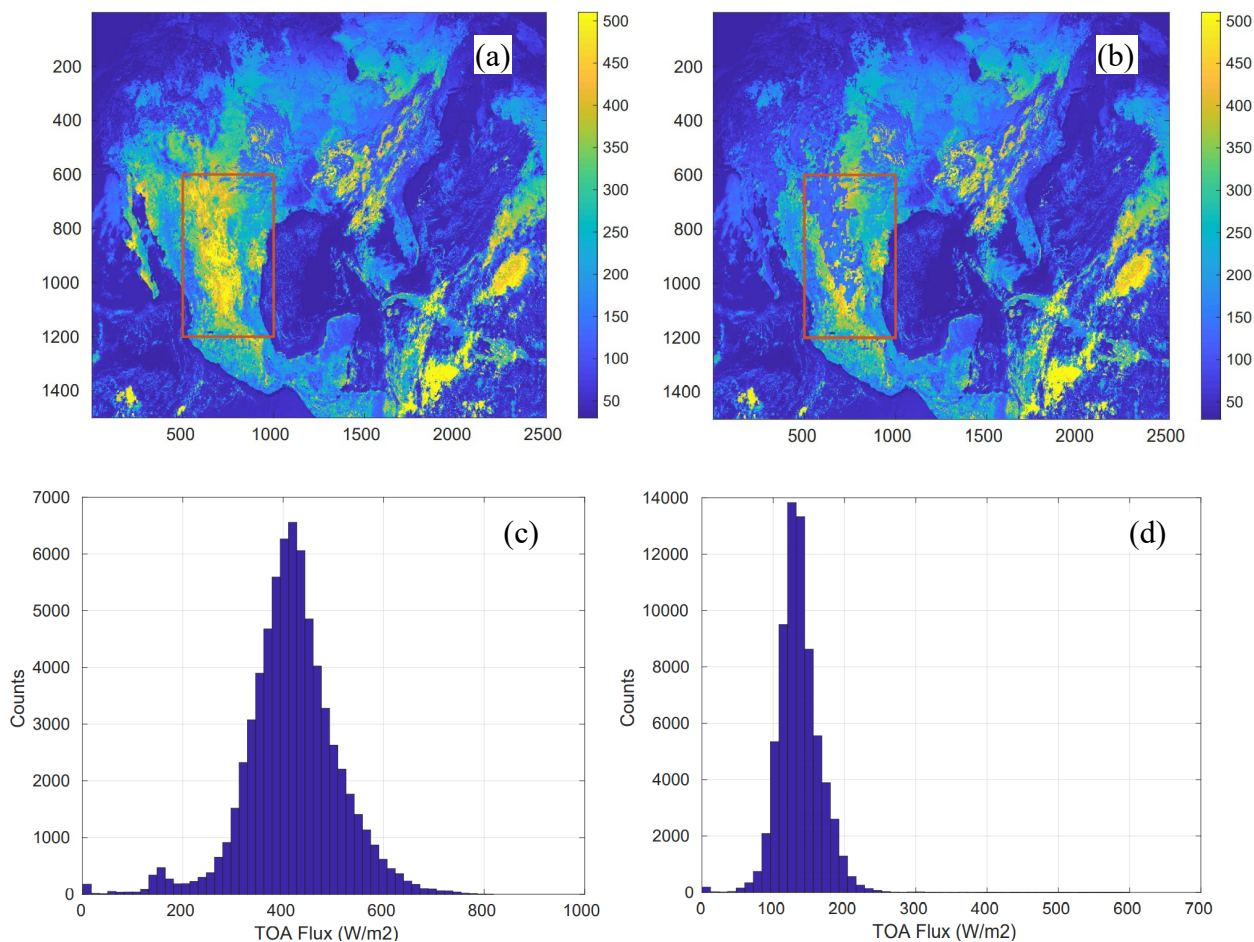
606 **Figure 14.** *Left:* Sensor response function for ABI channel 6; *Right:* Spectral albedo for desert and open  
607 shrubs. Desert albedo value is much higher than open shrubs at 2.2 μm.

608

609



610



611

612 **Figure 15.** TOA fluxes using two different NTB coefficients: *Left*: used “open shrub” coefficients;  
613 *Right*: “Desert” coefficients. Lower panels show the frequency distribution of TOA fluxes for a reduced  
614 domain (over Mexico in the orange boxes) that includes the open shrub/desert classification. Case time  
615 stamp is 2017/11/25 17:32Z.

616

617

618